https://ntrs.nasa.gov/search.jsp?R=20170008482 2020-05-10T01:14:23+00:00Z

SMAP L-band Microwave Radiometer: Instrument Design and First Year on Orbit

Jeffrey R. Piepmeier, *Senior Member, IEEE,* Paolo Focardi, *Senior Member, IEEE,* Kevin Horgan, *Member, IEEE*, Joseph Knuble, Negar Ehsan, *Member, IEEE,* Jared Lucey, Clifford Brambora, Paula R. Brown, Pamela J. Hoffman, Richard T. French, Rebecca L. Mikhaylov, Eug-Yun Kwack, Eric M. Slimko, Douglas E. Dawson, Derek Hudson, Jinzheng Peng, Priscilla Mohammed, *Member, IEEE,* Giovanni De Amici, Adam P. Freedman, James Medeiros, Fred Sacks, Robert Estep, Michael W. Spencer, Curtis W. Chen, Kevin B. Wheeler, Wendy N. Edelstein, Peggy O'Neill, *Fellow, IEEE,* Eni G. Njoku, *Fellow, IEEE*

ABSTRACT

Abstract – The Soil Moisture Active Passive (SMAP) L-band microwave radiometer is a conical scanning instrument designed to measure soil moisture with 4% volumetric accuracy at 40-km spatial resolution. SMAP is NASA's first Earth Systematic Mission developed in response to its first Earth science decadal survey. Here, the design is reviewed and the results of its first year on orbit are presented. Unique features of the radiometer include a large 6-meter rotating reflector, fully polarimetric radiometer receiver with internal calibration, and radio-frequency interference detection and filtering hardware. The radiometer electronics are thermally controlled to achieve good radiometric stability. Analyses of on-orbit results indicate the electrical and thermal characteristics of the electronics and internal calibration sources are very stable and promote excellent gain stability. Radiometer NEDT < 1 K for 17-ms samples. The gain spectrum exhibits low noise at frequencies >1 mHz and $1/f$ noise rising at longer time scales fully captured by the internal calibration scheme. Results from sky observations and global swath imagery of all four Stokes antenna temperatures indicate the instrument is operating as expected.

I. Introduction

National Aeronautics and Space Administration's (NASA's) Soil Moisture Active Passive (SMAP) satellite was launched into a 685-km near sun-synchronous 6AM/PM orbit on January 31, 2015. SMAP's L-band microwave radiometer was commissioned in February and March and has now reached its milestone of one year of successful operation. A three-dimensional rendering of the SMAP observatory in its fully deployed configuration is shown in Fig. 1. SMAP is the third in a series of modern L-band radiometers after the European Space Agency's (ESA) Soil Moisture Ocean Salinity (SMOS) satellite launched in 2009 and NASA's Aquarius instrument aboard Argentina's Comisión Nacional de Actividades Espaciales (CONAE) Satelite de Aplicaciones Cientificas (SAC)-D satellite launched in 2011 [1]-[3]. SMAP's primary science objective is to provide soil moisture measurements with an uncertainty < 0.04 m^3m^{-3} for terrain having vegetation water contents up to 5 kg/m^2. For the radiometer, this objective requires radiometric uncertainty < 1.3 K (with fore and aft averaging) with < 40-km spatial resolution.

SMAP is NASA's first Earth Systematic Mission developed in response to its first Earth science decadal survey [4]. The SMAP mission high-level science requirements and derived instrument requirements related to the radiometer are shown in Table 1 (adapted from [5]). Early in its mission, SMAP provided 10-km resolution soil moisture globally every three days using a combined active-passive microwave instrument. The instrument comprises a radiometer and a synthetic aperture radar (SAR), which both share a single antenna. In July, the radar ceased transmissions and has remained in receive-only mode since [6]. By itself the radiometer enables 40-km resolution soil moisture with the same three-day global coverage. Nonetheless, with its conical-scanning (real aperture) antenna

and advanced RFI mitigation capabilities, the SMAP radiometer is providing high-quality brightness temperature measurements of Earth's land, ice and ocean surfaces.

TABLE 1. SMAP RADIOMETER SCIENCE AND INSTRUMENT REQUIREMENTS.

Scientific Measurement Requirements	Instrument Functional Requirements
Soil Moisture: 0.04 m^3m^{-3} volumetric uncertainty (1-σ) in the top 5 cm for vegetation water content ≤ 5 kg m^{-2}; Hydroclimatology at 40-km resolution	L-Band Radiometer (1.41 GHz): Polarization: V, H, T_3 and T_4 Project 3-dB beamwidth ≤ 40 km Radiometric Uncertainty ≤ 1.3 K Constant 40° incidence angle
Sample diurnal cycle at consistent time of day (6am/6pm Equator crossing); Global, 3-day (or better) revisit	Swath Width: 1000 km Minimize Faraday rotation
Observation over minimum of three annual cycles	Baseline three-year mission life

The two key technology innovations – the large scanning 6-meter reflector and the total power radiometer receiver with advanced RFI detection and filtering capabilities – combined make the SMAP radiometer unique. On-orbit results of SMAP's RFI mitigation capabilities are discussed in [7]. In other ways, the SMAP radiometer derives its requirements and/or design from past radiometer systems. The front-end architecture with a 6-meter antenna shared with the radar was inherited from the preliminary design of the Hydrosphere State (Hydros) Earth System Science Pathfinder (ESSP) mission, which was selected as an alternate ESSP by NASA but did not proceed with development in 2005 [5]. SMAP's antenna is conical scanning with a full 360-degree field of regard. However, there are several key differences (some unique) from previous low-frequency conical scanning radiometers like WindSat or Advanced Microwave Scanning Radiometer for the Earth Observing System (AMSR-E) [8][9]. Most obvious is the lack of external warm-load and cold-space reflector, which normally provides radiometric calibration through the feed horn. Rather, SMAP's internal calibration scheme is based on the Jason Microwave Radiometer, the Aquarius push broom radiometers and the SMOS radiometer using

reference load switches and coupled noise diodes [9]-[11]. Switching of the internal calibrations sources is synchronized with the radar operation, as it is on Aquarius, so the radiometer oversamples the footprint. Both SMAP and Aquarius utilize this oversampling technique for time-domain detection and filtering of radio-frequency interference [12][13]. Like WindSat, SMAP measures all four Stokes parameters with fore and aft viewing; unlike WindSat, SMAP uses coherent detection for the third and fourth Stokes parameters implemented in a digital receiver backend [14]. The first two modified Stokes parameters, T_V and T_H, are the primary science channels used by the soil moisture retrieval algorithm [15]. The T_3 channel measurement provides correction of Faraday rotation caused by the ionosphere [16]. The T_4 channel is measured as a consequence of the receiver design and the data are used to detect RFI. The most significant difference SMAP has from all past space borne radiometer systems is its aggressive hardware and algorithm approach to RFI detection and filtering [13][7]. The requirement to detect and filter RFI drives and exploits features of the SMAP design.

Here, the main features of the SMAP radiometer design, results of early orbit operations, and observations for the first year up through March 2016 are presented. Section II covers the observatory, swath and antenna design. Section III describes the radiometer electronics and their calibration before launch. Activities and results of pre-launch calibration and early operations on-orbit are discussed in Sections IV and V. A review of one year of data is discussed in Sections VI & VII.

II. Observatory and Antenna Design

SMAP orbits Earth at 685-km altitude with the spacecraft pointing to geodetic nadir. The instrument antenna points 35.5° away from nadir and generates a 2.4° 3-dB beamwidth for the radiometer. This geometry creates an instantaneous field-of-view (IFOV) of 36-by-47 km with an Earth incidence angle (EIA) of 40°. The distance across the swath is 1000 km from IFOV center-to-center. This swath width, combined with the orbit parameters, allows the whole of Earth's surface to be covered in three days (except for typical pole holes) with no gaps at the equator.

Imaging is accomplished by conical scanning the antenna beam with a full 360° field of regard. The antenna rotates at 14.6 rpm completing a scan with 3200-km circumference every 4.1 seconds. Along-scan averaging occurs over 14-ms, which smears the beam along scan to create a 39-by-47 km effective field-of-view (EFOV). Along-scan sampling occurs every 11 km, which is faster than the 20-km Nyquist criterion. With the spacecraft moving at 6.8 km/s speed over ground, the along track (or across scan) sampling at center of swath is 28 km – slightly slower than the 24-km Nyquist criterion. The spatial sampling geometry near center of swath is shown in Fig. 2.

The instrument antenna, shared between the radiometer and the SAR, is composed of a 6-m offset reflector fed by a dual polarized, dual band feed-horn. With a focal length of 4.2 m and a projected diameter of 6 m, a Kevlar net shapes the deployable mesh reflector into a triangularly faceted surface with an RMS error compared to a perfect paraboloid less than 2mm or about 1% wavelength. Optimized for both the radiometer (1.4015-1.4255 GHz) and the SAR (1.2168-1.2982 GHz) frequency bands, the feed-horn includes an Ortho-Mode-Transducer (OMT) to separate horizontal and vertical polarizations. The OMT is

partly made of titanium to thermally isolate the horn, which is exposed to the thermal radiation environment, from the radiometer electronics.

Fig. 3 shows a comparison between the CAD model of the SMAP observatory with the reflector fully deployed and its RF model used to predict the antenna performance. All significant details relative to 21-cm wavelength were included into the model to get the best possible accuracy in the radiation pattern. The reflector antenna radiation pattern was not measured before launch; therefore, a very accurate antenna pattern knowledge was required to verify performance requirements (e.g., beam efficiency) and for the initial radiometer calibration. A 1/10th scale model replicating all major aspects of the flight hardware was also designed, built and tested to validate the RF model. Final requirement verification was then done with a combination of flight feed assembly measurements, scale model predictions and measurements and flight model predictions. A horizontal polarization pattern cut along the along-scan direction (horizontal direction) is plotted in Fig. 4. The main lobe has a half-power beamwidth of 2.4 degrees. The backlobes, primarily due to feed pattern spillover and edge diffraction, fall into the space region. The beam efficiency for vertical and horizontal polarizations is 88%, with most of the non-main lobe contribution directed towards space.

III. Radiometer Electronics Design

The radiometer electronics consist of antenna feed network, radiometer front end (RFE), radiometer back end (RBE), and radiometer digital electronics (RDE). These subsystems are shown in Fig. 5 with signal flow from right to left. The antenna feed network includes an external noise source and diplexers to separate radar frequencies

from the radiometer path. The external noise source signal is added to the antenna signal, but is not used as a primary calibration source and is present for redundancy. The diplexers include additional filtering to limit the amount of RFI entering the RFE. The RFE contains the primary internal calibration switches and noise source, RF amplification and additional filtering. The internal noise source signal is added to the reference signals to provide RFI-free gain calibration. The RBE down-converts the RF signals to a lower IF frequency using a common phase-locked local oscillator (PLO). The reference clock for the PLO also clocks the analog-to-digital converters (ADCs) in the RDE. The ADCs sample and quantize the IF signals for processing by a Field Programmable Gate Array (FPGA)-based Digital Signal Processor (DSP). The DSP generates detected power for the full passband (fullband data) and for 16 channels spaced evenly across the passband (subband data). The RDE generates timing signals needed to control the internal calibration sources and synchronizes radiometer integration with the radar timing. Finally, data are packetized by the RDE and sent to spacecraft mass storage for later downlink to the ground.

The RF system is designed to make linear radiometric measurements in the presence of RFI up to an Interference-to-Noise Ratio (INR) of 6 dB or an effective added noise temperature of 2000 K due to RFI out of a typical 500 K system temperature. Above 2000 K, the accumulators in the integrator logic saturate. Cascaded filtering and amplification sufficient to operate each stage at a maximum power of 24-dB below 1-dB compression keeps the error contribution from nonlinearity due to RFI signals negligible over this range. The total system frequency response is shown in Fig. 6. Note, the response is 30 dB below peak at the allocation edges at 1400 MHz and 1427 MHz. The roll-off to

>100 dB is much faster on the low side because of the presence of air search radars and less stringent on the high side because of fewer known RFI sources.

The digital backend replaces conventional diode detectors with moment accumulators and complex cross-correlators. The first four moments of the ADC outputs are estimated by the RDE. The science-processing algorithm computes the second central moment using the first and second moments to estimate the total power [17]. These data are used to estimate antenna temperature. The kurtosis (used by the RFI detectors) is computed in a similar manner using raw moments. The complex cross-correlation coefficient is also measured by the RDE and is used in the science-processing algorithm to estimate third and fourth Stokes parameters.

Third and fourth Stokes parameters are measured by the radiometer to compensate for Faraday polarization basis rotation caused by the ionosphere and to be used as RFI detectors. The driving requirement on the receiver was to minimize (relative to 24-MHz bandwidth) differential group delay between the vertical and horizontal channels. Because the complex correlation is measured, any mean phase difference between vertical and horizontal polarizations can be compensated by a complex coefficient multiplication in the science-processing algorithm. Phase slope difference, however, would attenuate the correlation between signals, and is minimized in the design by using symmetry and avoiding unnecessarily long cables of different lengths.

The radiometer integrator logic operates synchronously with the radar whereby the radiometer integrates received power during the radar receive window and blanks during the transmit window. Timing is shown in Fig. 7. The fundamental unit of integration is 300 μs contained within a pulse-repetition interval (PRI). Fullband data are integrated at this

rate. Subband data, however, are integrated 1.2 ms over a packet defined as four PRI's. During a footprint, eight (8) packets are utilized to view earth for 9.6 ms and four (4) packets to view the internal reference load and noise source or calibration for 4.8 ms. Because of a small amount of blanking during radar transmit and calibration switching setup time, this cycle occurs on a 17 ms period.

The radiometer timing, antenna beamwidth and scan rate, and ground software averaging are coordinated so the equivalent low-pass processes work together to produce Nyquist sampled footprints along the scan direction. The frequency responses of the processes are shown in Fig. 8. The on-board integrators are represented by the two rightmost traces (dash-dot and dash) for 1 and 4 PRI's, respectively. The 8-packet (32-PRI) integration done in ground software to form a footprint has a low-pass response indicated by solid trace labeled L1B_TB. The Level 1 product footprint process has a 3-dB point at 30 Hz, which fully samples the low-pass process created by the antenna pattern sweeping across the earth. The bump in the footprint response near 100 Hz is caused by the interleaving of antenna looks with calibration looks, which robs integration time from the scene. A balance is struck in the algorithm design between increased NEDT and vs. decreased $\Delta G/G$ noise. The high-frequency energy at 100 Hz in the antenna averaging response is merely white noise aliased into the footprints and equivalent to the increase in NEDT due to limiting antenna integration time. Finally, the dotted line marked "antenna" shows the equivalent low-pass response of the antenna approximated by a Gaussian beam (sweeping along-scan in azimuth at 770 km/sec speed over ground) to naturally occurring thermal radiation.

The four packets of calibration observations are partitioned into two packets for reference load and two packets for reference plus noise diode. Conventionally, noise is injected prior to a reference switch; however, on SMAP as on Aquarius, RFI is such a concern that the noise injection is done behind the switch to ensure the radiometer can be calibrated regardless of RFI entering the antenna. The noise source on SMAP, unlike Aquarius, is a single noise source split coherently between the vertical and horizontal receiver channels. This method was chosen because the digital receiver has negligible cross-polarization coupling and the total power and cross-correlation detectors can be calibrated essentially independently. The phase of the correlated noise source was set at 40° to enable calibration of the real and imaginary outputs of the correlator using the same calibration state.

The radiometer science-processing algorithm uses these pairs of reference and noise diode counts to compute gain and offset coefficients, which are then further averaged over a longer time period (multiple footprints) to reduce estimation noise. The gain and offset are computed twice per footprint in the science-processing algorithm and then averaged with a 5000-tap, uniform, centered non-causal filter. The frequency responses of these filters are discussed in the on-orbit data section below. Careful attention was paid to thermal control to allow gain and offset coefficient averaging over 10's of seconds and to help maintain radiometer stability on orbital and seasonal time-scales. The combination of passive thermal design with an active proportional controller achieves 0.1^{o}C/orbit within the RFE [22][23]. Worst-case orbital results are also discussed in the on-orbit results section below.

IV. Pre-Launch Calibration

The pre-launch calibration of the radiometer includes both a radiometric and a polarimetric exercise to characterize temperature dependence of the reference and noise source looks and receiver phase imbalance relative to the feedhorn input. The radiometric calibration was accomplished using techniques similar to [18] and polarimetric calibration [19]. The goal of the radiometric calibration is to characterize the losses (or equivalent) and noise diode added noise temperature, represented by the simplified loss model shown in Fig. 9, for use in the science-processing algorithm. Likewise, the goal of the polarimetric calibration is to determine the polarimetric efficiency and phase differences of the receiver channels.

In the science-processing algorithm, the antenna temperature referenced to the feedhorn output/OMT input is computed from radiometer output counts using a two-point calibration model:

$$T'_A = T'_{ref} - \frac{c_{ref} - c_A}{c_{ND,R} - c_{ref}} T'_{ND} \tag{1}$$

where $T'_{,ref}$ is the internal reference load noise temperature and $T'_{,ND}$ the coupled noise source temperature referred to the feedhorn output/OMT input. The radiometer output counts are represented by c_x, where x indicates reference (*ref)*, antenna (A), and noise diode + reference (*ND,R*) states. The intermediate antenna temperature (1) is input-referred to the feedhorn aperture by correcting for feed and radome losses and physical temperatures:

$$T_A = L_{radome} L_{feed} T'_A - L_{radome}\left(L_{feed} - 1\right) T_{feed} - (L_{radome} - 1) T_{radome} \tag{2}$$

where L_x and T_x are the loss factors and physical temperatures for x equal to the *radome* and *feed*. The internal calibration temperatures can be expressed as functions of the lumped losses and physical temperatures shown in the loss model Fig. 9:

$$T'_{ref} = L_{OMT}L_{coup}L_{dip}T_{RFE} - L_{OMT}L_{coup}\left(L_{dip} - 1\right)T_{dip} \tag{3a}$$

$$-L_{OMT}\left(L_{coup} - 1\right)T_{coup} - (L_{OMT} - 1)T_{OMT}$$

$$T'_{ND} = L_{OMT}L_{coup}L_{dip}L_{switch}T_{ND} \tag{3b}$$

Alternately, (3a) and (3b) can be approximated using a linear model:

$$T'_{ref} = T_{\mathrm{RFE}} + c_{\mathrm{RFE},\mathrm{ref}}\Delta T_{\mathrm{RFE}} + c_{\mathrm{OMT},ref}\Delta T_{\mathrm{OMT}} + c_{\mathrm{coup},ref}\Delta T_{\mathrm{coup}} + c_{\mathrm{dip},ref}\Delta T_{\mathrm{dip}} + T_{offset} \tag{4a}$$

$$T'_{\mathrm{ND}} = T_{,ND} + c_{\mathrm{RFE},ND}\Delta T_{\mathrm{RFE}} + c_{\mathrm{OMT},ND}\Delta T_{\mathrm{OMT}} + c_{\mathrm{coup},ND}\Delta T_{\mathrm{coup}} + c_{\mathrm{dip},ND}\Delta T_{\mathrm{dip}} \tag{4b}$$

where coefficients c_x are derived from pre-launch thermal vacuum (TVAC) testing and ΔT_x indicates physical temperature deviation away from the reference temperature used in the linear model fitting.

The TVAC tests consisted of a series of data collections with the radiometer at different combinations of controlled temperatures for each zone. The first TVAC test was limited to the radiometer electronics and the coaxial components portion of the feed network. Each major component was installed on an individually controlled heater plate, were connected together using spaceflight coaxial cables, and temperatures were then varied ±10°C about 20°C after [20]. A coaxial calibration source comprising a temperature stabilized matched termination and coldFET was used to provide two-point calibration. The coldFET was calibrated against a liquid nitrogen coaxial standard load. A second TVAC test was performed with the OMT and feedhorn installed viewing a flat ferrite tile absorber plate. While data taken in the first were used to obtain the sensitivity of the coupler, diplexer and the internal calibration sources to their physical temperature, the second test

yielded the sensitivity of the calibration to OMT and feedhorn temperatures. The resulting calibration coefficients are shown in Table 2. There is a relative lack of sensitivity of the reference load antenna-referred temperature due to variations in feed network components; however, the reference load temperature is quite sensitive to changes in the RFE temperature as indicated by the 20% value of c_{RFE}, likely due to changes in thermal gradients. The noise source has a temperature sensitivity of $c_{RFE}/T_{ND} = 2.5$ and 2.7 ppt/°C due to RFE temperature changes for the vertical and horizontal polarization channels, respectively.

Table 2 SMAP Radiometer Calibration Coefficients (Full Band)

		c_{RFE}	c_{OMT}	c_{coup}	c_{dip}	Note
T'_{ref}	V-pol	0.205	4.78×10^{-5}	-0.052	-0.073	T_{offset} =0.225 K
	H-pol	0.208	5.23×10^{-5}	-0.056	-0.064	T_{offset} =0.741 K
T'_{ND}	V-pol	1.18	0.015	0.036	0.002	T_{ND} = 465 K
	H-pol	1.24	0.012	0.053	0.048	T_{ND} = 452 K

The radiometer's complex cross correlator is used to measure third and fourth Stokes parameters. The radiometer has a symmetric design, but the two polarization channels are not necessarily phase balanced or spectrally balanced. A digitally controlled correlated noise source with adjustable phase was used to determine that the polarimetric efficiency of the system was effectively unity (0.999). The two channels have the same passband response and negligible group delay difference. Nonetheless, as the received

signals propagate along the receiver channels, the relative correlation angle will be changed, as the receiver's channel phase imbalance is nonzero. Scattering parameter measurements versus temperature indicate phase imbalance is quite stable. For example, the RFE inter-channel phase imbalance varies 0.03°/°C. This amount is negligible considering performance of the thermal control system. Thus, phases were measured at room temperature using different techniques during integration and calibration of the radiometer.

First, network analyzer measurements show the internal calibration noise diode, which is imbedded inside the RFE, has a phase imbalance (from the RFE input to output) of 1.6°. Positive sign means that the v-pol channel has longer equivalent electrical length. The path lengths between the RFE and RDE are unequal, creating an additional -41° phase shift, which was measured by network analyzer and verified using the radiometer correlator. Finally, to calibrate the channel phase imbalances in the radiometer before the RFE inputs, a polarizing grid over LN2 calibration target was used. The principle of this test is to create linearly polarization radiation at the feedhorn input. Rotating the grid generates a third Stokes parameter with a correlation coefficient rotated by the receiver's total phase imbalance in the complex plane. Excluding the channel phase imbalance after the RFE inputs, the channel phase imbalance from the feedhorn to the RFE inputs is 39°. These phase differences are used in the science-processing algorithm to produce third and fourth Stokes antenna temperatures.

V. Early On-Orbit Activities

The stowed configuration of the SMAP antenna offers an unobstructed view of deep space to the feedhorn (see Fig. 10). The radiometer was powered on Feb. 12, 2015 to take advantage of the stowed configuration. Using this well known calibration point, one calibration parameter in the radiometer can be adjusted. The noise source was chosen because it has the largest uncertainty remaining from pre-launch calibration testing. Estimated cold space antenna temperatures were expected to be approximately 4 K ± 9 K (3-σ) based on pre-launch calibration parameters and their uncertainties. The noise source pre-launch uncertainty of 1% is largely responsible for errors in this configuration. Other error sources include internal reference load temperature, front-end component loss, and antenna feed pattern uncertainties. A typical orbit of antenna temperature measurements is shown in Fig. 11. The results based on pre-launch calibration for V-pol are 5 K too low; however, after noise source correction, the measured antenna temperature matches the expected cold-space antenna temperatures quite well. The H-pol results showed only 1 K initial discrepancy and similar agreement after correction. The radiometer was powered off on Feb. 13 to prepare for reflector deployment.

After accomplishing the space view, the reflector was deployed in a static configuration. The radiometer was powered on again Feb. 27-28, 2015 to provide information to aid reflector deployment verification. The reflector was pointed aft of the spacecraft and the nadir angle was predicted to be slightly smaller than that when spinning because of boom deflection due to centrifugal force. The results of this test were favorable.

Both brightness temperature response and NEDT measurements are as expected. As shown in Fig. 12, brightness temperature response over land, ice, and ocean are reasonable

(note the color scale is limited to emphasize variations over land). High brightness temperatures are seen over rain forest in South America and West Africa and desert in North Africa and Middle East. NEDT values estimated by the science-processing algorithm are 0.8 K and 1.1 K over ocean and land, respectively. These values are consistent with instrument design specifications.

On March 31, 2015, the radiometer reflector was rotating at operational speed and the instrument electronics were powered back on. After a check out period, the radiometer was declared operational. It has been operating successfully since.

VI. First Year on Orbit

The radiometer error budget is dominated by NEDT because of the narrow time-bandwidth product (9.6 ms by 24 MHz) available to the system. The orbit average NEDT for all four Stokes antenna temperatures is shown in Fig. 13 during the first year of operation. The orbit average NEDT is consistent with an average over land, ocean and ice scenes and is stable throughout the year with mean value 0.90 K and 0.96 K for horizontal and vertical polarization, respectively. The NEDT for third and fourth Stokes parameters is 1.34 K, which is approximately the expected factor of $\sqrt{2}$ larger than NEDT for vertical and horizontal polarizations.

Transient temperatures, particular those that cause changes in thermal gradients within the RFE, can cause drift in systematic calibration biases (in scale and/or offset). While the science-processing algorithm compensates for temperature effects, the model has residual uncertainty. The radiometer is thermally stabilized by passive thermal design and active thermal control to minimize the impacts of the changing thermal environment.

Several platinum resistance thermometers (PRTs) are used to measure the temperatures and thermal stability of the radiometer components. The PRT measurements of the front-end over the first year are shown in Fig. 14. Each PRT is read every 20 seconds and has 0.01°C resolution and ±0.5°C accuracy. During most of the past year and when under normal operating conditions the temperatures are quite stable. The diplexers, couplers, and OMT are seen to vary <1°C seasonally including during the south-pole solar eclipse season (May through July) in panel (a). Even if left uncompensated, the variation in calibration bias due to these front-end thermal variations is <0.1 K. The feed horn varies in temperature quite a bit more, about 14°C peak-to-peak, but its ohmic loss is nearly negligible and varies 2ppm/°C. The temperatures of the internal calibration sources has 0.4°C peak-to-peak variation shown in panel (b). The internal noise source has a temperature coefficient of 3 ppt/°C (referred to the feedhorn), which results in a calibration dependence of 0.3 K that is compensated in the science-processing algorithm. The steps in temperature early in the operation year are due to various activities during the first two weeks of instrument commissioning. The occasional 1°C impulses are due to instrument power cycling as a consequence of satellite operations. These power cycles do interrupt the calibration temporarily; however, the instrument recovers within a few orbits and returns to steady state thereafter.

The short-term orbital variations in temperature are shown in Fig. 15 for the worst-case peak of the eclipse season. During this orbit the feedhorn varied 2°C and the other feed network components 0.2°C. The internal calibration sources varied 0.1°C over the orbit. These variations have negligible impact on the intra-orbital stability of the receiver calibration.

Noise diode bias current and avalanche breakdown voltage are measured every 8 days during normal operations and plotted in Fig. 16. The bias current is stable to 2μA peak-to-peak and breakdown voltage 1.4mV peak-to-peak. Based on laboratory measurements of diode components, the calibration dependence on these DC bias variations is 250 ppm.

The combination of noise diode bias stability and thermal stability lead to excellent radiometer gain stability on orbital time scales. The radiometer switching provides noise diode and reference load counts every 8.4 ms. These are used to compute gain and offset coefficients with some corrections applied for temperature. The calibration coefficients are then averaged with a 5000-tap moving average window spanning 42 seconds of elapsed time. Thus, it is necessary for the hardware gain to be stable with periods < 84 seconds so the process Nyquist samples the hardware behavior. The gain spectrum and averaging filter response are shown in Fig. 17. The gain is stable ($<<10^{-5}$) above 1 mHz (1000-second period) so the 42-second filter is averaging over small fluctuations. The orbit period of 5900 seconds is marked for reference. The temperature correction algorithm compensates for orbital-scale dependence in gain. Below 1 mHz, the gain spectrum begins to rise with $f^{-\alpha}$ type behavior; however, this characteristic is fully captured by the calibration scheme.

Noise diode calibration sources are known to drift on long timescales while on orbit (e.g., [24]) and this behavior was no exception on SMAP's precursor Aquarius, which exhibited an exponential drift with 0.5% amplitude and 100-day time constant [25]. Noise source drift of 0.5% is equivalent to 1 K drift over the ocean. The calibration drift over land due to noise source drift is less because the land antenna temperatures are closer to the internal reference load temperature. SMAP uses the same basic design as Aquarius for the

noise sources, so long-term drift is expected and is being monitored. Because of the potentially long time constant of 100 days, it is too early to determine if SMAP is exhibiting exactly similar behavior. Nonetheless, SMAP stability is monitored against a globally averaged ocean model (based on that described in [26]) with results reported in [27]-[29]. Calibration drift cast as a relative change in noise diode intensity is plotted in Fig. 18. The lower curve shows the estimated drift including several steps downward and upward due to intentional and unintentional power cycles of the radar transmitter. The upper curve is an estimate of the drift due to changes in radiometer hardware over the year with the steps removed. The vertical dashed lines indicate the start and finish of solar eclipse season for the spacecraft during the southern hemisphere winter. The bump downwards in calibration immediately after eclipse ends is likely due to some uncompensated front-end thermal effect. As discussed in [27]-[29], there remains uncertainty in radome and reflector emissivity that is confounded with noise source drift. The separation of the errors and correction thereof are topics of on-going calibration activities. Nonetheless, the stability of SMAP is consistent with Aquarius, although the physical mechanisms and temporal characteristics are not yet fully resolved.

VII. Stokes Imagery

SMAP provides global coverage with a 3-day revisit on an 8-day repeat orbit cycle. Antenna temperature data averaged over one such cycle for all four modified Stokes parameters are shown in Fig. 19. These data are during the third week of April 2016 from [20]. The impact of moisture in the soil on antenna temperature in Fig. 19 (a) vertical and (b) horizontal polarizations is quite evident across the northern hemisphere, including the

Midwest and the State of Texas in the United States where extreme precipitation led to flooding resulting in low brightness temperatures 180-190 K shown in blue on the cool end of the color scale. Other physical features of note include the high emissivity of the Amazon rainforest and the dry Sahara shown in red at the warm end of the color scale. Note, the color scale was truncated at (168-282 K) to emphasize contrast in antenna temperature of land. This truncation necessarily saturates at ocean antenna temperatures, where dominance of Fresnel reflectivity would otherwise be evident in contrast between vertical and horizontal polarizations. Strong contrast, however, is seen in regions of sea ice with 190 and 230 K antenna temperatures at horizontal and vertical polarizations, respectively.

The third Stokes antenna temperature Fig. 19 (c) shows a strong dipole feature caused by ionospheric Faraday rotation. The dipole in third Stokes arises from alignment of earth's magnetic field with direction of propagation of observed microwave emission. The amplitude of third Stokes is strongest over ocean because of the low emission and strong polarization caused by its Fresnel reflectivity and weaker over land (especially Amazon and Congo rainforests) due to higher emissivity and depolarization due to scattering. There are also artifacts in the image due to combining ascending and descending orbits. The fourth Stokes parameter, on the other hand, is nearly non-existent in Fig. 19 (d). The color scale is slightly offset to account for a global bias, likely due to antenna cross-polarization mixing. The continents are slightly more negative than ocean and their outlines are evident because of antenna cross-pol mixing, which couples some combination of first and second into fourth Stokes. Finally, there are unique patterns of fourth Stokes antenna temperature over Greenland and Antarctica, perhaps vestiges of the polarimetric signature witnessed by WindSat [30].

VIII. Discussion

One year of nearly continuous operation of the SMAP L-band microwave radiometer was marked on March 31, 2016. Two key technologies – the 6-meter scanning reflector and the RFI detection and filtering digital backend with polarimetric capabilities – combine to make the radiometer unique. Radiometer footprints sampled at 17-ms provide angular Nyquist sampling and exhibit NEDT <1 K. On-board calibration combined with good thermal stability yields excellent on-orbit gain stability. Global swath imagery of all four Stokes antenna temperatures shows good results. Vertical and horizontal polarized channels display expected behavior for land, ocean and ice scenes. The third Stokes channel responds strongly to ionospheric Faraday rotation. The fourth Stokes channel indicates little circularly polarized emission, except over large ice sheets. The instrument continues to operate equally well as of this writing. Thus, the radiometer meets the key and driving mission requirements needed to measure soil moisture at 40-km spatial resolution and 0.04 volumetric uncertainty.

Acknowledgments

SMAP is managed for NASA's Science Mission Directorate in Washington by JPL, with instrument hardware and science contributions made by NASA's Goddard Space Flight Center in Greenbelt, Maryland. JPL built the spacecraft and is responsible for project management, system engineering, radar instrumentation, mission operations and the ground data system. Northrop Grumman Astro Aerospace Division made the reflector and boom assembly. Goddard is responsible for the radiometer instrument and science data products.

References

[1] D. Entekhabi, E.G. Njoku, P.E. O'Neill, et al., "The Soil Moisture Active Passive (SMAP) Mission," *Proc. IEEE*, Vol. 98, No. 5, pp. 704-716, May 2010.

[2] Kerr, Y. H. et al., ``The SMOS Mission: A New Tool for Monitoring Key Elements of the Global Water Cycle,'' *Proc. IEEE*, vol. 98, pp. 666-687, 2010.

[3] G. Lagerloef et al., "The Aquarius/SAC-D Mission: Designed to Meet the Salinity Remote Sensing Challenge," *Oceanography*, vol. 21, no. 1, pp. 68–81, Mar. 2008.

[4] National Research Council. *Earth Science and Applications from Space: National Imperatives for the Next Decade and Beyond.* Washington, DC: The National Academies Press, 2007. [Online]. Available: http://dx.doi.org/10.17226/11820.

[5] D. Entekhabi *et al.,* "The Hydrosphere State (Hydros) Satellite Mission: an Earth System Pathfinder for Global Mapping of Soil Moisture and Land Freeze/Thaw," *Trans. IEEE Geosci. Rem. Sens.*, vol.42, no. 10, pp. 2184-2195, Oct. 2004.

[6] "NASA Soil Moisture Radar Ends Operations, Mission Science Continues", *NASA/JPL*, 2016. [Online]. Available: http://www.jpl.nasa.gov/news/news.php?feature=4710. [Accessed: 28- Mar- 2016].

[7] P. N. Mohammed et al., "SMAP L-Band Microwave Radiometer: RFI Mitigation Prelaunch Analysis and First Year On-Orbit Observations," in *IEEE Trans. Geosci. Rem. Sens.*, vol. 54, no. 10, pp. 6035-6047, Oct. 2016.

[8] P.W. Gaiser *et al.,* "The WindSat Spaceborne Polarimetric Microwave Radiometer: Sensor Description and Early Orbit Performance," *Trans. IEEE Geosci. Rem. Sens.*, vol.42, no. 11, pp. 2347-2361, Nov. 2004.

[9] T. Kawanishi *et al.*, "The Advanced Microwave Scanning Radiometer for the Earth Observing System (AMSR-E), NASDA's contribution to the EOS for global energy and water cycle studies," *Trans. IEEE Geosci. Rem. Sens.*, vol. 41, no. 2, pp. 184-194, Feb. 2003.

[10] D.M. Le Vine, G.S.E. Lagerloef, F.R. Colomb, S.H. Yueh and F.A. Pellerano, "Aquarius: An Instrument to Monitor Sea Surface Salinity from Space," *Trans. IEEE Geosci. Rem. Sens.*, vol.45, no.7, pp.2040-2050, July 2007.

[11] S. Brown, C. Ruf , S. Keihm , A. Kitiyakara, "Jason Microwave Radiometer Performance and On-Orbit Calibration," *Marine Geodesy,* vol. 27, no. 1-2, pp.199-220, 2004.

[12] S. Misra and C. S. Ruf, ``Detection of radio frequency interference for the Aquarius radiometer,'' *IEEE Trans. Geosc. Rem. Sens.*, vol. 46, pp. 3123--3128, 2008.

[13] J.R. Piepmeier, J.T. Johnson, P.N. Mohammed, D. Bradley, C. Ruf, M. Aksoy, R. Garcia, D. Hudson, L. Miles, M. Wong, "Radio-Frequency Interference Mitigation for the Soil Moisture Active Passive Microwave Radiometer," in *Trans. IEEE Geosci. Rem. Sens.*, vol.52, no.1, pp.761-775, Jan. 2014.

[14] J.R. Piepmeier and Gasiewski, A.J., "Digital Correlation Microwave Polarimetry: Analysis and Demonstration," *Trans. IEEE Geosci. Rem. Sens.*, vol.39, no.11, pp.2392-2410, Nov. 2001.

[15] P. E. O'Neill, E. G. Njoku, T. J. Jackson, S. Chan, and R. Bindlish, "SMAP Algorithm Theoretical Basis Document: Level 2 & 3 Soil Moisture (Passive) Data Products," Jet Propulsion Laboratory, California Institute of Technology, Pasadena, CA, JPL D-66480, 2015. [Online.] Available at http://nsidc.org/data/docs/daac/smap/sp_l2_smp/index.html

[16] S.H. Yueh, "Estimates of Faraday rotation with passive microwave polarimetry for microwave remote sensing of Earth surfaces," *Trans. IEEE Geosci. Rem. Sens.*, vol.38, no.5, pp.2434-2438, Sep 2000.

[17] Piepmeier, J. R. et al. SMAP Algorithm Theoretical Basis Document: L1B Radiometer Product. SMAP Project, NASA GSFC SMAP-ALGMS-RPT-006 Rev. B, NASA Goddard Space Flight Center, Greenbelt, MD. Feb. 2016. [Online.] Available at http://nsidc.org/data/docs/daac/smap/sp_l1b_tb/index.html

[18] C.S. Ruf, S.J. Keihm and M.A. Janssen, "TOPEX/POSEIDON microwave radiometer (TMR): I. Instrument description and antenna temperature calibration," *IEEE Trans. Geosci. Remote Sens.,* vol. 33, pp. 125–137, Jan. 1995.

[19] J. Peng and C. S. Ruf, "Calibration Method for Fully Polarimetric Microwave Radiometers Using the Correlated Noise Calibration Standard," in *IEEE Trans. Geosci. Rem. Sens.*, vol. 46, no. 10, pp. 3087-3097, Oct. 2008.

[20] Johnson, Chris, "Temperature Stability and Control Requirements for Thermal Vacuum/Thermal Balance Testing of the Aquarius Radiometer," 25th Space Simulation Conference, Annapolis, MD, October 20-23, 2008.

[21] Piepmeier, J. R., P. Mohammed, J. Peng, E. J. Kim, G. De Amici, and C. Ruf. 2015. *SMAP L1B Radiometer Half-Orbit Time-Ordered Brightness Temperatures, Version 3*. [March 31-April 3, 2015]. Boulder, Colorado USA. NASA National Snow and Ice Data Center Distributed Active Archive Center. http://dx.doi.org/10.5067/VIQYQV0AJATI.

[22] Mastropietro, A.J., et al., "Preliminary Evaluation of Passive Thermal Control for the Soil Moisture Active Passive (SMAP) Radiometer," 41st International Conference on Environmental Systems (ICES), 2011, AIAA 2011-5070.

[23] Mikhaylov, R., E. Kwack, R. French, D. Dawson, and P.J. Hoffman, "Implementation of Active Thermal Control (ATC) for the Soil Moisture Active and Passive (SMAP) Radiometer," 44th International Conference on Environmental Systems (ICES), 2014, ICES-2014-060.

[24] Brown, S.T., S. Desai, W. Lu and A. Tanner, "On the Long-Term Stability of Microwave Radiometers Using Noise Diodes for Calibration," in *IEEE Trans. Geosci. Rem. Sens.*, vol. 45, no. 7, pp. 1908-1920, May 2007.

[25] Piepmeier, J.R., L. Hong and F.A. Pellerano, "Aquarius L-Band Microwave Radiometer: 3 Years of Radiometric Performance and Systematic Effects," *IEEE Trans. Geosci. Rem. Sens.,* vol.8, no.12, pp.5416-5423, Dec 2015.

[26] F. J. Wentz and D. M. LeVine, "Algorithm theoretical basis document: Aquarius salinity retrieval algorithm," Remote Sensing Systems, Santa Rosa, CA, USA, RSS Tech. Rep. 082912, 2012 [Online]. Available FTP: ftp://podaac-ftp.jpl.nasa.gov/allData/aquarius/docs/v2/AQ-014-PS-0017_AquariusATBD_Level2.pdf

[27] J.R. Piepmeier et al., *SMAP Radiometer Brightness Temperature Calibration for the L1B_TB and L1C_TB Beta-Level Data Products*, NASA's SMAP Project, Jet Propulsion Laboratory, Pasadena, CA. Jul. 2015. [Online.] https://nsidc.org/data/smap/data_versions.

[28] J.R. Piepmeier et al., *SMAP Radiometer Brightness Temperature Calibration for the L1B_TB and L1C_TB Version 2 Data Products*, NASA's SMAP Project, Jet Propulsion Laboratory, Pasadena, CA. Nov. 2015. [Online.] https://nsidc.org/data/smap/data_versions.

[29] J.R. Piepmeier et al., *SMAP Radiometer Brightness Temperature Calibration for the L1B_TB and L1C_TB Version 3 Data Products*, NASA's SMAP Project, Jet Propulsion Laboratory, Pasadena, CA. Apr. 2016. [Online.] https://nsidc.org/data/smap/data_versions.

[30] Li, L., P. Gaiser, M. R. Albert, D. G. Long and E. M. Twarog, "WindSat Passive Microwave Polarimetric Signatures of the Greenland Ice Sheet," *IEEE Trans. Geosci. Rem. Sens.*, vol. 46, no. 9, pp. 2622-2631, Sept. 2008.

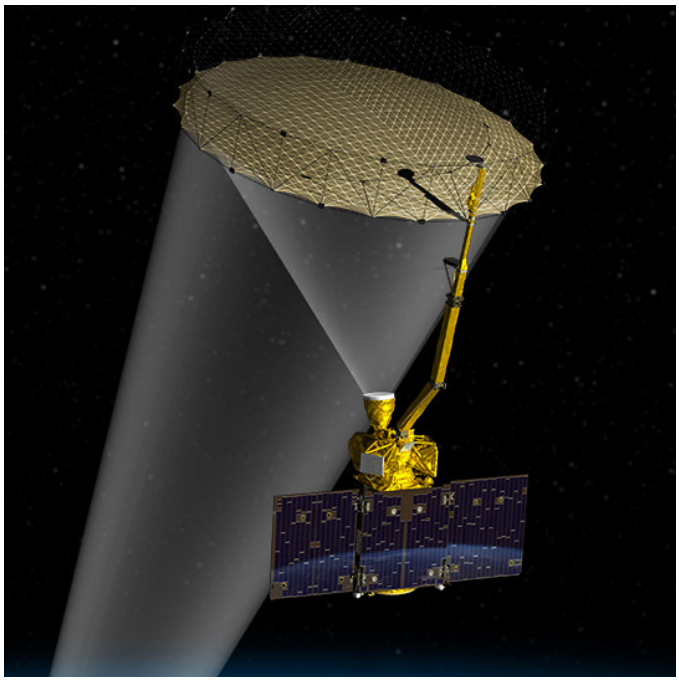

Fig. 1. Soil Moisture Active Passive (SMAP) observatory in fully deploy configuration. Image Credit: NASA/JPL-Caltech.

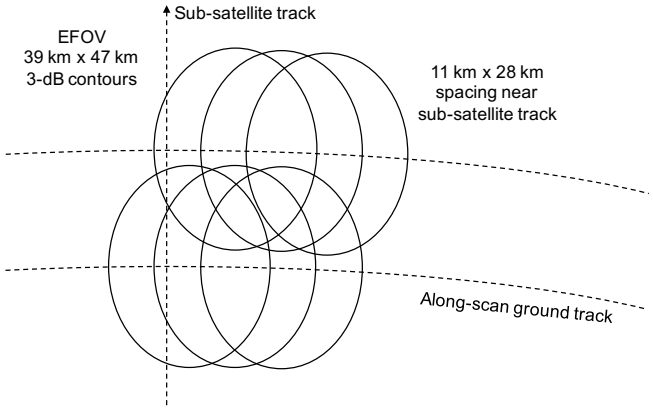

Fig. 2. Footprint spacing near sub-satellite track.

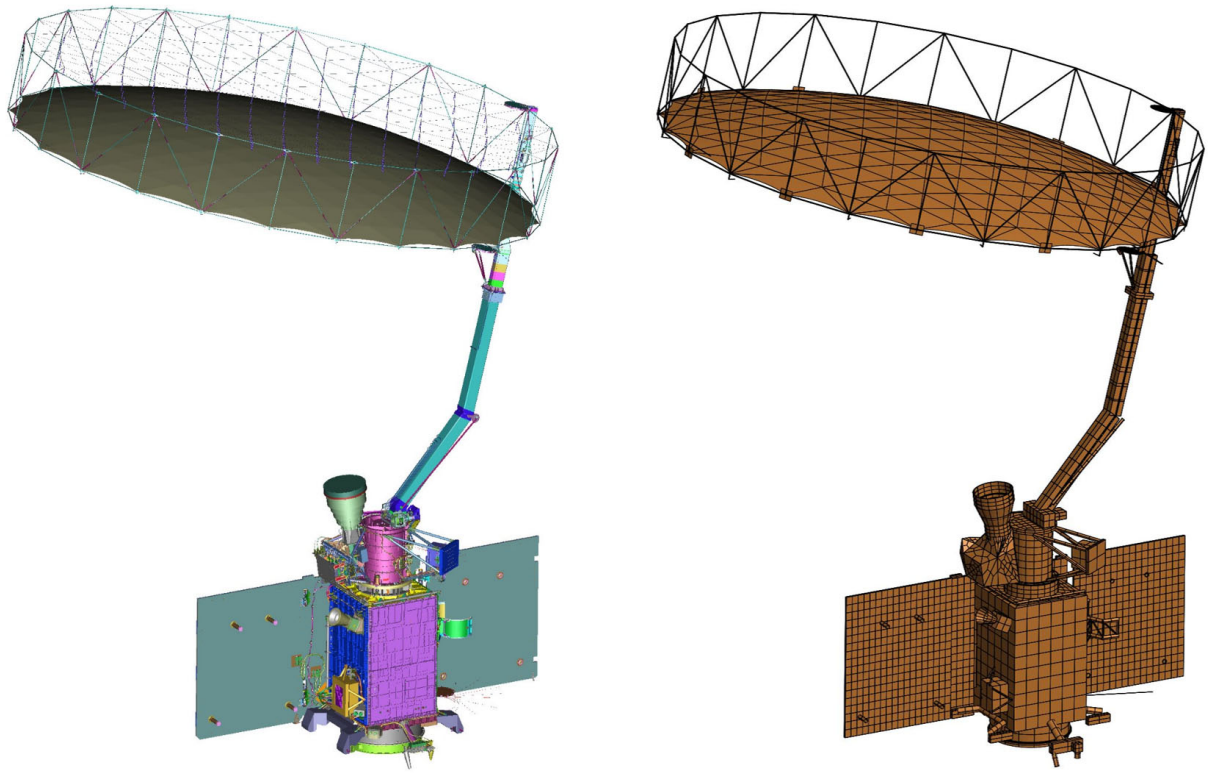

(a) (b)

Fig. 3. SMAP observatory (a) solid model from mechanical design software and (b) mesh model for 3D antenna analysis software.

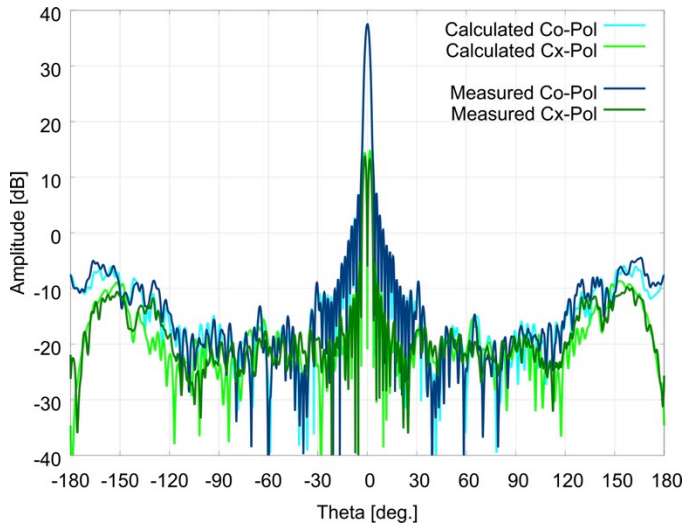

(a)

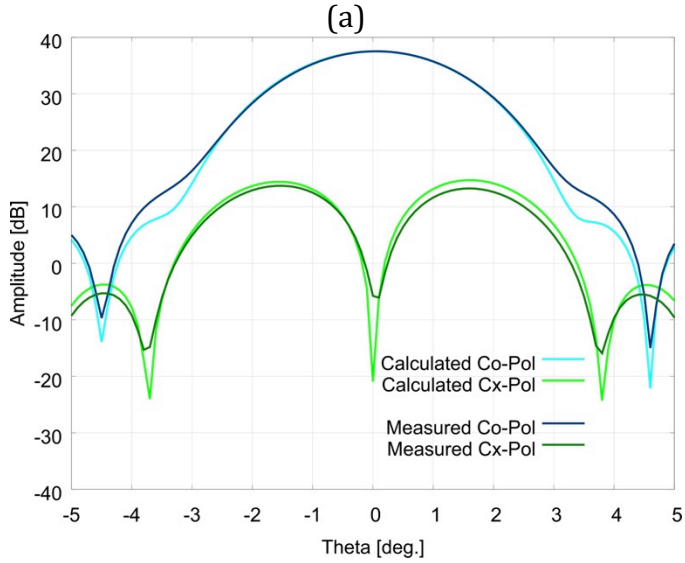

(b)

Fig. 4. Antenna pattern cut of horizontal polarization along the antenna scanning direction for (a) the full pattern and (b) the main lobe. Comparison is between calculated and measured data for the 1/10 SMAP scale model.

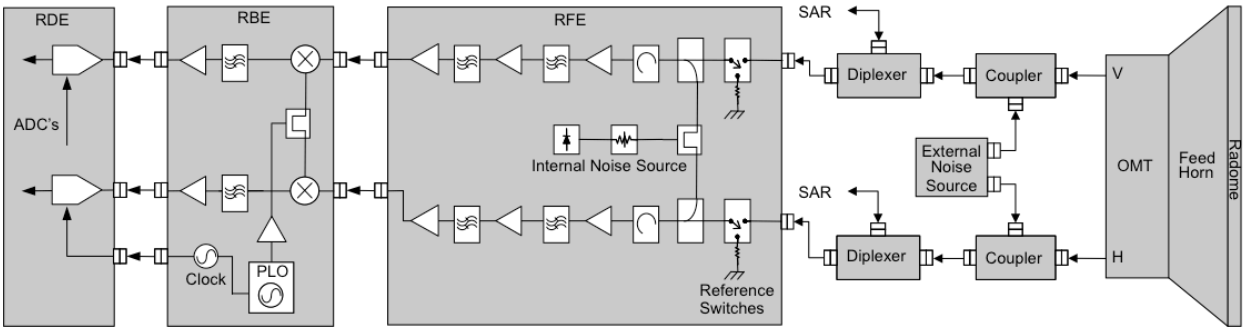

Fig. 5. Radiometer Block Diagram including feed network, Radiometer Front-End (RFE), Back-End (RBE), and Digital Electronics (RDE). Signal flow is from right to left.

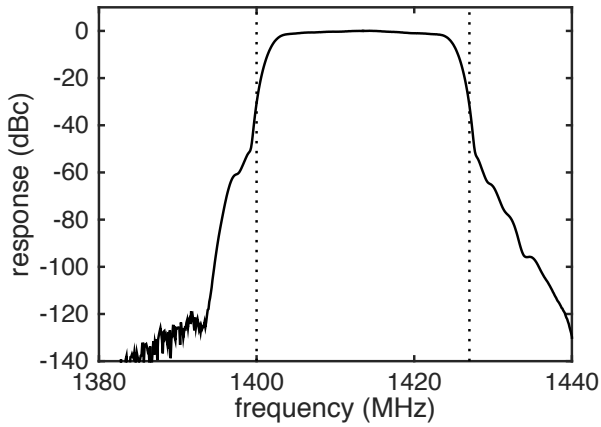

Fig. 6. Frequency response of SMAP microwave radiometer. This response combines RF, IF and digital filters. Vertical dotted lines indicate the spectrum allocation at 1400 to 1427 MHz.

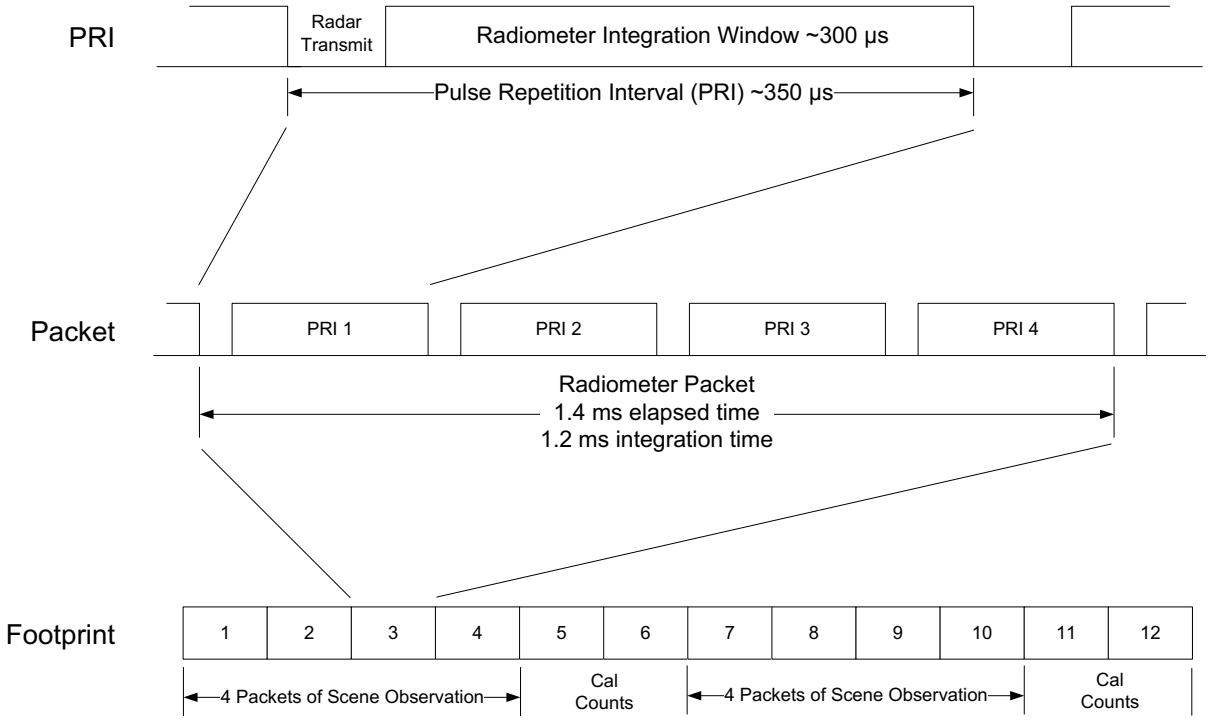

Fig. 7. Timing of radiometer sampling for a PRI, a packet, and a footprint.

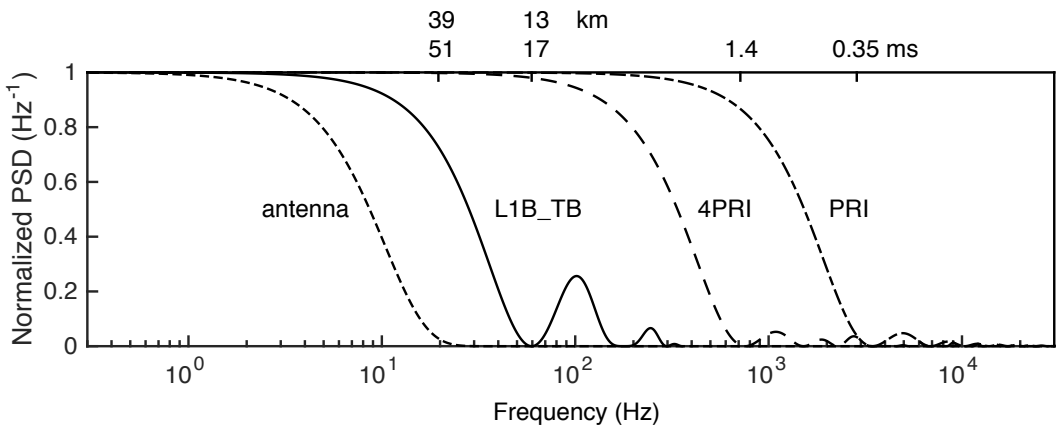

Fig. 8. Representative frequency response of averaging performed in radiometer operation and processing. The two rightmost traces (dash-dot and dash) show the low-pass response of the on-board boxcar integrator over one and four PRI, respectively. The solid trace shows the frequency response of the calibrated antenna temperatures found in the Level 1B_TB data product. Finally, the dotted line marked "antenna" shows the equivalent low-pass response of the antenna beam (sweeping along-scan in azimuth) to naturally occurring thermal radiation.

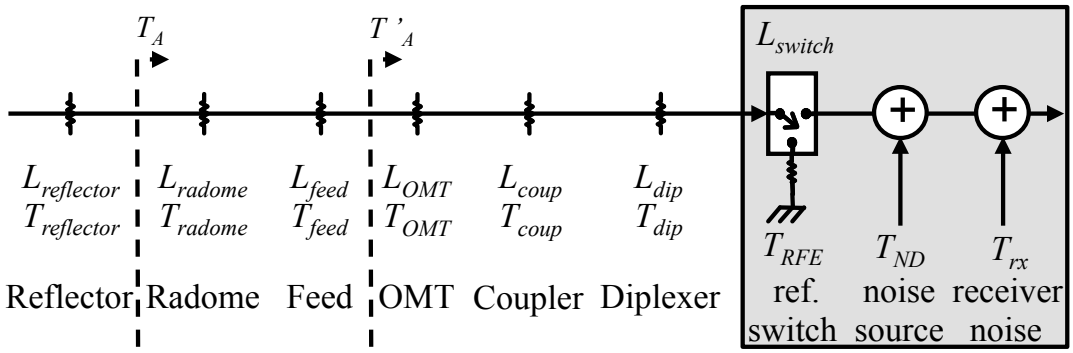

Fig. 9. Simplified calibration model showing lumped losses and physical temperatures.

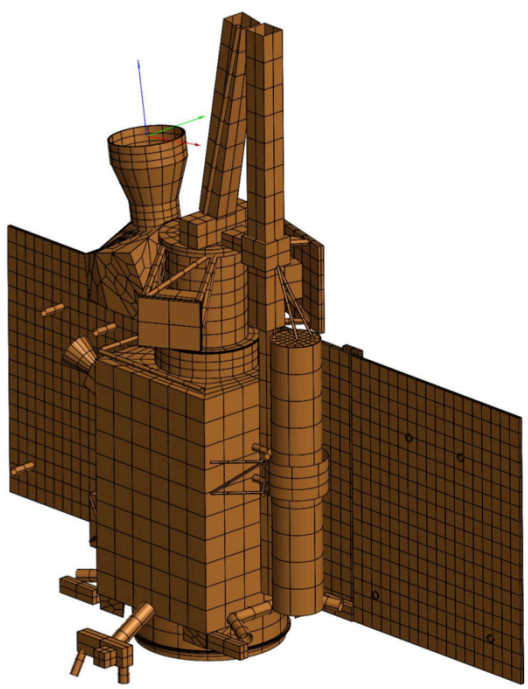

Fig. 10. Spacecraft model shows feedhorn viewing cold space with stowed reflector.

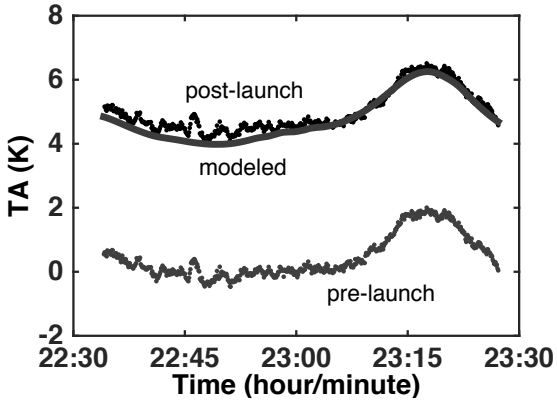

Fig. 11. Antenna temperature (V-pol) measured in stowed configuration showing pre- and post-launch calibration results compared to modeled cold-space antenna temperature . The initial result is biased 5 K low consistent with pre-launch calibration uncertainty. H-pol measurements showed a smaller 1-K difference.

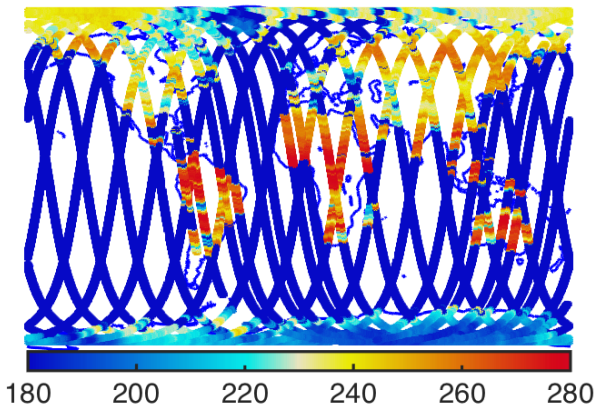

Fig. 12. Horizontally polarized brightness temperature (K) measured with static (non rotating) antenna. Width of the swath is 40-km and is exaggerated here for clarity.

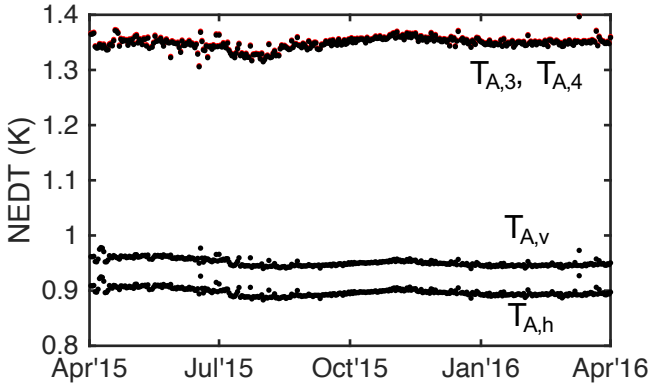

Fig. 13. Radiometric resolution (NEDT) daily averaged (over land, ocean, and ice) during first year of operations for all four Stokes brightness temperatures. The third and fourth Stokes parameters (top curves) have NEDT $\sqrt{2}$ larger than vertical and horizontal polarizations as expected.

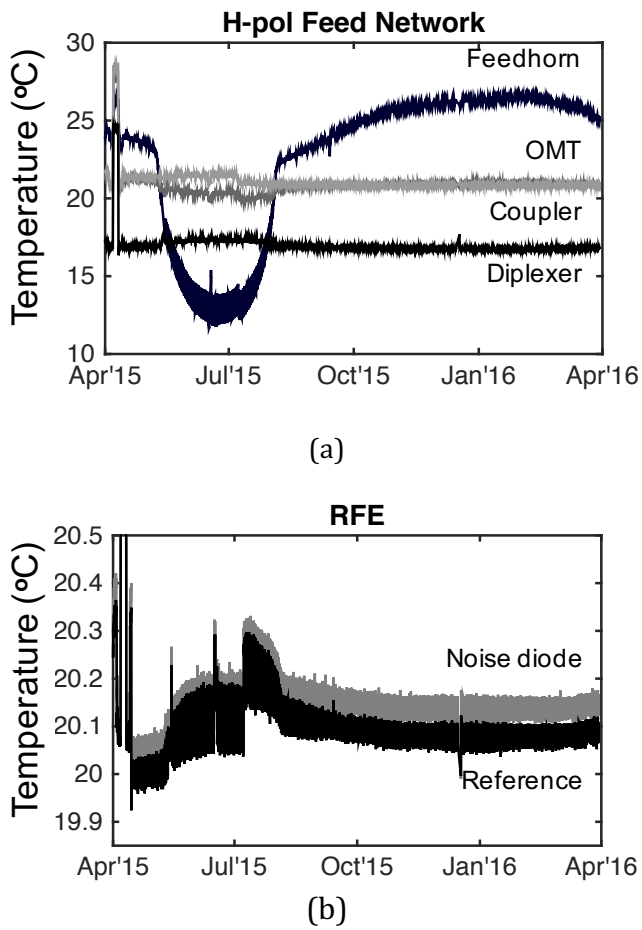

Fig. 14. Temperatures of (a) feed network and (b) internal reference load and noise source for horizontal-polarization during first year of operations.

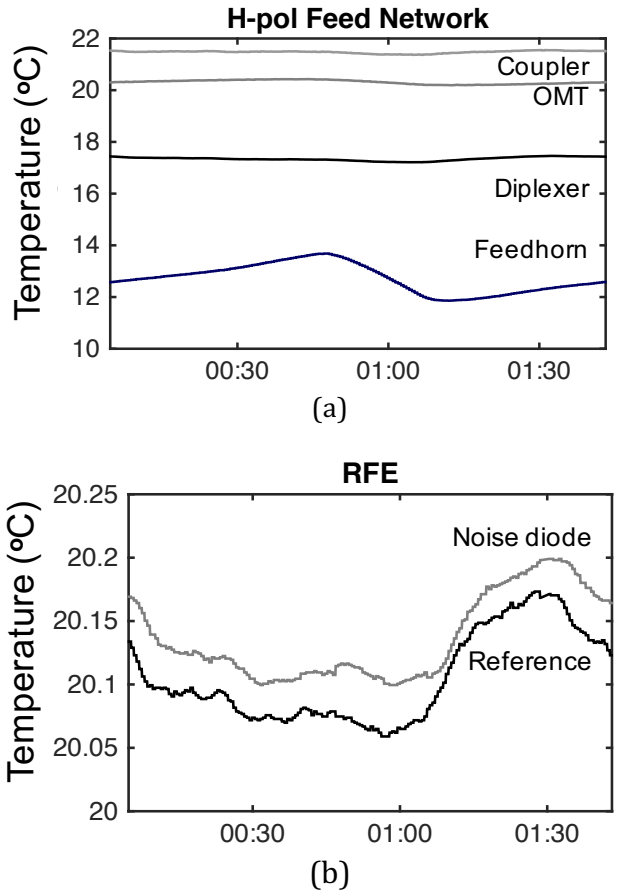

Fig. 15. Temperatures of (a) feed network and (b) internal reference load and noise source for horizontal-polarization over on orbit on June 23, 2015 near the peak thermal effect of eclipse season.

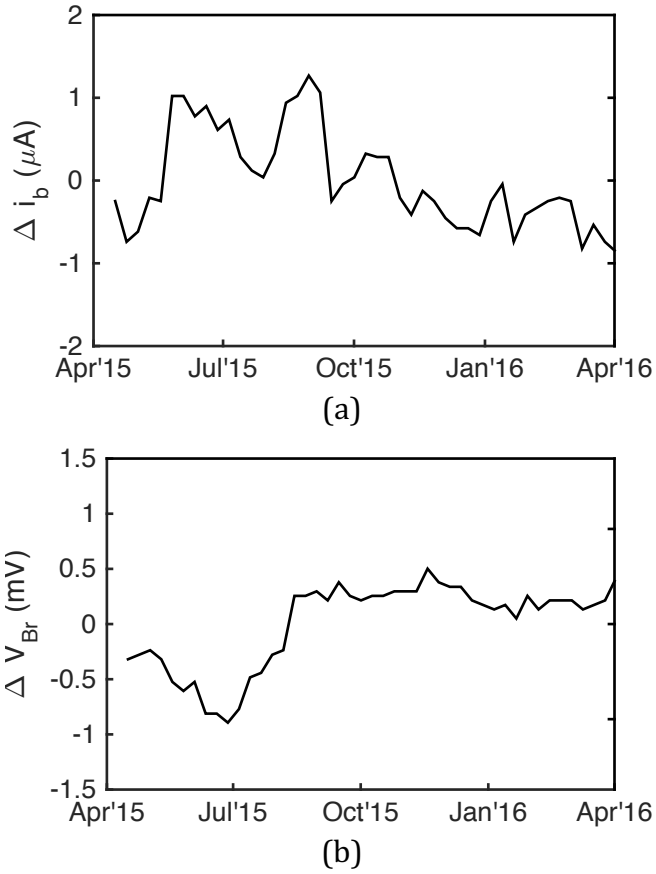

Fig. 16. Noise source bias history measured on an 8-day period during first year of operations. (a) Current bias variation is within ±1.1μA or ±180ppm and (c) avalanche voltage varies ±0.7mV or ±80ppm.

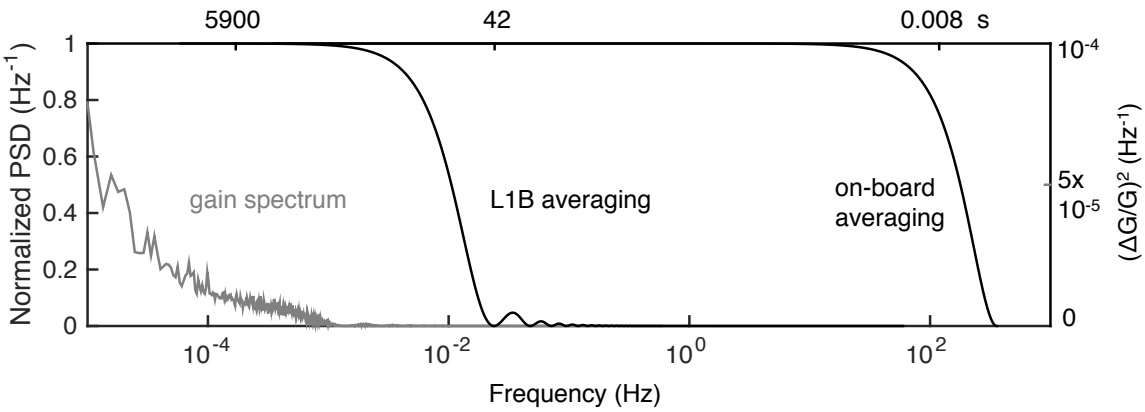

Fig. 17. Radiometer gain stability and gain averaging filter responses. The rightmost trace is the response of the on-board sampling of noise-diode and reference counts every 8.4 ms. The science processing software averages 5000 gain estimates together, which span 42 seconds. The orbit cycle is marked at 5900 seconds. The spectrum of gain coefficient fluctuation, the left most trace, reveals an increasing spectrum below 1 mHz.

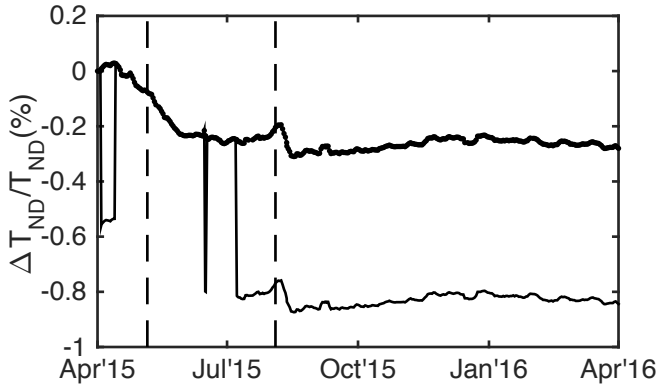

Fig. 18. Radiometer calibration stability cast as gain drift during first year of operation determined from comparison to globally-averaged ocean model (lower curve). The two steps in April are due to intentional change in physical temperature during early commissioning activities. The step near June 14 was due to an intentional power cycle. The final large step in July is due to termination of radar transmission. The upper curve is the same noise source drift with the radar-induced steps removed. The vertical dashed lines indicated the start and finish of solar eclipse season experienced by SMAP in the southern hemisphere winter.

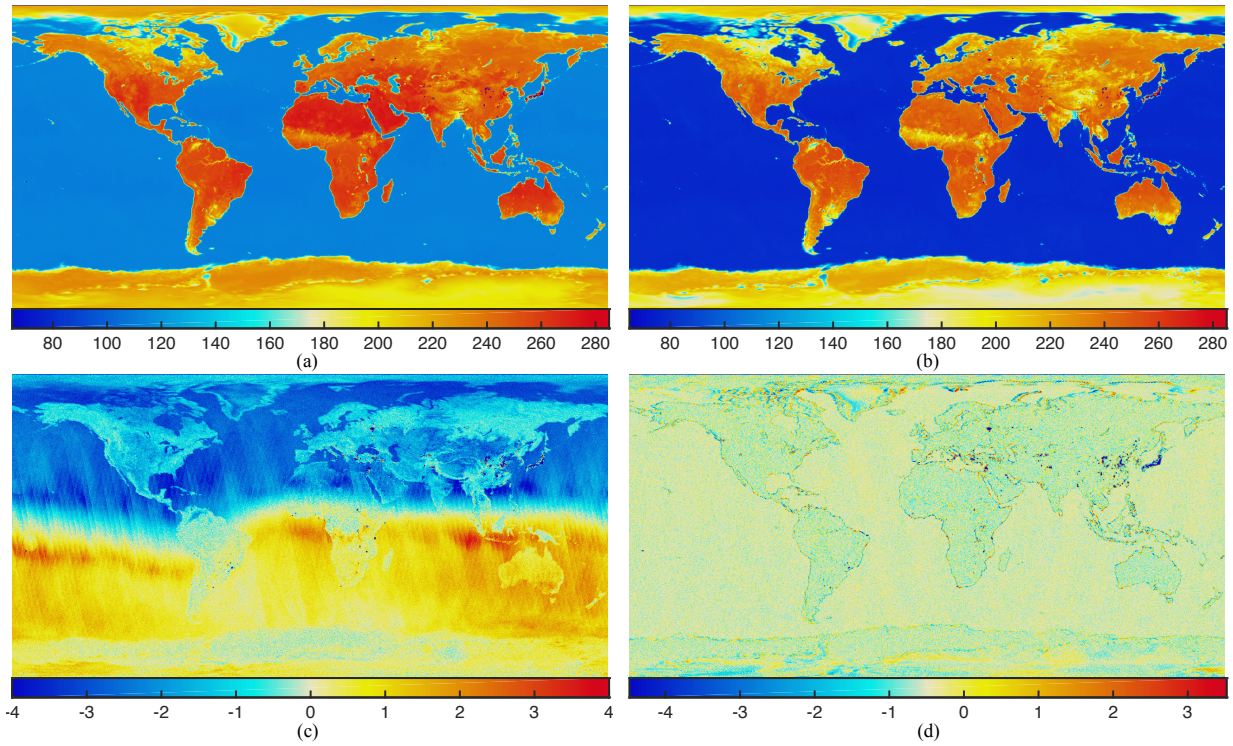

Fig. 19. SMAP radiometer modified Stokes antenna temperatures gridded and averaged during 1-7 September 2015. The four panels show (a) vertically polarized, (b) horizontally polarized, (c) third and (d) fourth Stokes parameters, respectively.